Construction and Experimental Implementation of a Model-Based Inverse Filter to Attenuate Hysteresis in Ferroelectric Transducers

Andrew G. Hatch, Ralph C. Smith, Tathagata De, and Murti V. Salapaka

***Abstract*—Hysteresis and constitutive nonlinearities are inherent properties of ferroelectric transducer materials due to the noncentrosymmetric nature of the compounds. In certain regimes, these effects can be mitigated through restricted input fields, charge- or current-controlled amplifiers, or feedback designs. For general operating conditions, however, these properties must be accommodated in models, transducer designs, and model-based control algorithms to achieve the novel capabilities provided by the compounds. In this paper, we illustrate the construction of inverse filters, based on homogenized energy models, which can be used to approximately linearize the piezoceramic transducer behavior for linear design and control implementation. Attributes of the inverse filters are illustrated through numerical examples and experimental open loop control implementation for an atomic force microscope stage.**

***Index Terms*—Atomic force microscopy (AFM), control systems, dielectric hysteresis, ferroelectric devices, modeling.**

I. Introduction

FERROELECTRIC materials, including the compound lead zirconate titanate (PZT), exhibit novel actuator and sensor capabilities due to the unique electromechanical coupling which they exhibit. This provides them with the capability for providing broadband transduction and nanometer-level set point accuracy. Furthermore, piezoelectric transducers are moderately inexpensive and can be designed to minimally affect the passive dynamics of underlying structures. However, the noncentrosymmetric ion structure that imbues the materials with unique actuator and sensor properties also produces hysteresis and constitutive nonlinearities at all drive levels.

To illustrate, consider the prototypical atomic force microscope (AFM) stage depicted in Fig. 1(a) which employs stacked piezoceramic actuators to position the sample in the x- and y-directions. An additional PZT mechanism provides transverse positioning capabilities. Nested minor loops collected at 0.1 Hz are plotted in Fig. 1(b) and data collected at frequencies ranging from 0.279 to 27.9 Hz is plotted in Fig. 2 to illustrate the frequency-dependent nature of the hysteresis inherent to field-displacement AFM data. The increased losses, as frequencies are increased, are due to three coupled phenomena: frequency-dependent dielectric losses, internal damping, and inertial dynamics of the actuator. As illustrated by PZT5A data in [31], the first mechanism produces a decrease in remanence or maximal strains output by the device. Due to the fully coupled nature of the phenomena, it is necessary to include all three mechanisms for accurate device characterization and model-based control design.

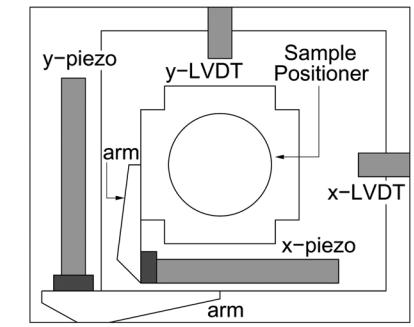

(a)

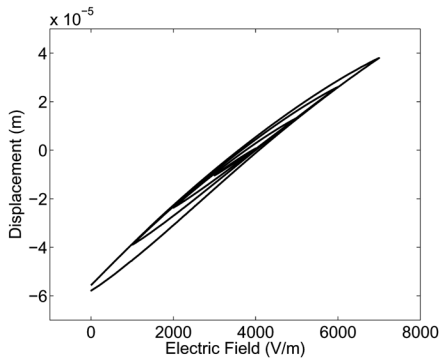

(b)

Fig. 1. (a) PZT-based AFM stage and (b) nested minor loops in data collected at 0.1 Hz.

At low frequencies, the inherent hysteresis can be accommodated through proportional–integral–derivative (PID) or robust control designs [6], [7], [18], [23]. However, at the higher frequencies required for applications ranging from

Manuscript received January 18, 2005; revised November 15, 2005. Manuscript received in final form June 12, 2006. Recommended by Associate Editor R. Moheimani. This work was supported by the National Science Foundation (NSF) under Grant CMS-0201560. The work of A. G. Hatch was supported by the Defense Advanced Research Projects Agency under Subcontract 1000-G-CF980. The work of R. C. Smith was supported in part by the NSF under Grant CMS-0099764 and by the Air Force Office of Scientific Research under Grants AFOSR-F49620-01-1-0107 and AFOSR-FA9550-04-1-0203.

A. G. Hatch and R. C. Smith are with the Department of Mathematics, Center for Research in Scientific Computation, North Carolina State University, Raleigh, NC 27695 USA (e-mail: aghatch@comcast.net; rsmith@eos.ncsu.edu).

T. De and M. V. Salapaka are with the Electrical Engineering Department, Iowa State University, Ames, IA 50011 USA (e-mail: tatha@iastate.edu; murti@iastate.edu).

Digital Object Identifier 10.1109/TCST.2006.883195

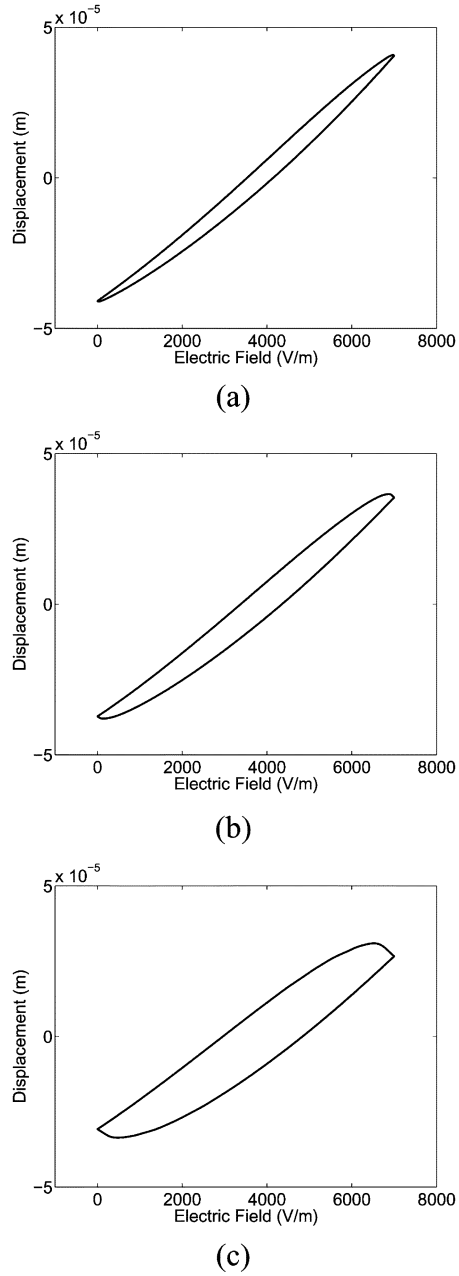

Fig. 2. Frequency-dependent field-displacement behavior of a stacked PZT stage: sample rates of: (a) 0.279, (b) 5.58, and (c) 27.9 Hz.

real-time monitoring of biological processes—e.g., protein unfolding—to comprehensive product diagnostics, increasing noise–to–data ratios and diminishing high-pass characteristics of control filters preclude a sole reliance on feedback laws to eliminate hysteresis. The latter difficulty is due in part to the very large gains required to attenuate uncompensated hysteresis and nonlinear dynamics. At low frequencies, these mechanisms are relatively benign and the use of high gains yields satisfactory performance. At high frequencies, however, the large gains augment discrepancies between the device behavior and that quantified by tractable models which often results in unstable closed-loop behavior.

Alternatively, it is illustrated in [15] and [16], that use of charge- or current-controlled amplifiers can essentially eliminate hysteresis. However, this mode of operation can be prohibitively expensive when compared with the more commonly employed voltage-controlled amplifiers, and current control is ineffective if maintaining dc offsets as is the case when the x-stage of an AFM is held in a fixed position while a sweep is performed with the y-stage.

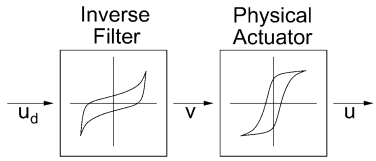

Fig. 3. Use of an inverse filter to linearize the response u of a hysteretic actuator to achieve a desired output u_d.

This motivates the development of models and model-based control designs which incorporate and accommodate the hysteresis and constitutive nonlinearities. Numerous approaches have been employed to characterize these nonlinear effects including Preisach models [9], [22], domain wall models [29], [30], micromechanical models [5], [13], [14], mesoscopic energy relations [4], [11], and homogenized energy models [27], [36]. We employ the homogenized energy framework due to its energy basis, its capability to quantify a wide range of physical phenomena and operating regimes, its unified nature for characterizing hysteresis in ferroelectric, ferromagnetic, and ferroelastic compounds [34], [35], and the potential it provides for real-time implementation. Details regarding the development of this modeling framework and its relation to other characterization techniques can be found in [25] and [36]. The manner in which the homogenized energy framework differs from Preisach models is detailed in Section II-C following the model description.

Model-based control design for piezoceramic transducers operating in highly hysteretic and nonlinear regimes can be roughly segregated into two categories: 1) nonlinear control designs and 2) linear control designs employing nonlinear inverse filters. Examples of the first technique in the context of optimal control design for smart material transducers, are provided in [24] and [39]. The second technique is based on the concept of employing either an exact or approximate inverse model to linearize the transducer behavior in the manner depicted in Fig. 3. This approach has been employed with a variety of models and control designs—e.g., see [12] and [37] for details regarding the development and implementation of control designs for magnetostrictive actuators using inverse relations for the Preisach operator and [38] for details regarding the development of adaptive control designs utilizing piecewise linear Preisach models and their inverses—and is the technique which we focus on in this paper.

In Section II, we summarize constitutive relations developed in [25] and [36] for ferroelectric materials and provide a highly efficient algorithm for implementing the model when thermal relaxation is negligible. A corresponding inverse polarization-field algorithm is summarized in Section III and illustrated through a numerical example. The constitutive model is subsequently employed in Section IV to develop a lumped model for the stacked actuator employed in the AFM stage shown

in Fig. 1(a) to illustrate the construction of a macroscopic transducer model. The accuracy of the transducer model is illustrated through a comparison with the frequency-dependent data plotted in Fig. 2. In Section V, an algorithm for the inverse displacement-field relation to linearize the transducer response is developed and, in Section VI, the algorithm is experimentally implemented as an inverse filter for the open-loop tracking of a triangular input signal. It is demonstrated that this model-based filter design effectively linearizes the nonlinear and hysteretic transducer dynamics and provides an approximately tenfold increase in accuracy at higher frequencies as compared with the unfiltered case. This significantly improves the accuracy of the transducer and diminishes the sole reliance on feedback laws whose authority decreases as tracking speeds and noise–to–data ratios increase.

II. Constitutive Relations

Constitutive relations quantifying the electromechanical behavior of piezoceramic materials are constructed in two steps. In the first, Helmholtz and Gibbs energy relations at the lattice level are used to characterize the local field-polarization and field-strain behavior of ferroelectric compounds for thermally inactive and active operating regimes. In the second step of the development, material nonhomogeneities and variable effective field effects are incorporated through the assumption that certain material properties are manifestations of underlying distributions rather than constants. This yields low-order macroscopic constitutive relations which are efficient to implement.

A. Local Constitutive Relations

Let E, P, ε, and σ, respectively, denote the electric field, polarization, strain, and stress. It is illustrated in [36] that an appropriate formulation of the Helmholtz energy for fixed temperatures in the absence of stresses is

$$\psi_P(P) = \begin{cases} \frac{1}{2}\eta(P+P_R)^2, & P \le -P_I \\ \frac{1}{2}\eta(P-P_R)^2, & P \ge P_I \\ \frac{1}{2}\eta(P_I-P_R)\left(\frac{P^2}{P_I}-P_R\right), & |P| < P_I. \end{cases}$$

As shown in Fig. 4, P_I is the positive inflection point which delineates the transition between stable and unstable regions, P_0 denotes the unstable equilibrium, and P_R is the value of P at which the positive local minimum of ψ occurs. The parameter η is the reciprocal of the slope of the E–P relation after switching occurs. This fact can be used to establish an initial parameter value for η when modeling a specific data set.

Details regarding the development of Helmholtz energy relations based on statistical mechanics tenets can be found in [25] and [36]. Whereas less efficient to implement, these relations yield kernels that accommodate the noncongruency measured in certain operating regimes.

The corresponding Gibbs energy relation

$$G_P(E,P) = \psi_P(P) - EP \tag{1}$$

incorporates the electrostatic energy due to the applied field E when $\sigma = 0$.

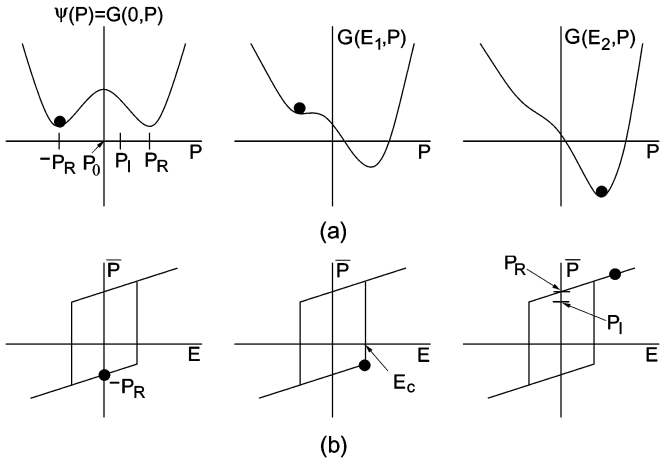

Fig. 4. (a) Helmholtz energy ψ and Gibbs energy G for $\sigma = 0$ and increasing fields E. (b) Switch in the local polarization $\overline{P}$ that occurs as E is increased beyond the local coercive field E_c given by (5) in the absence of thermal activation.

Elastic effects and electromechanical coupling are incorporated in the Helmholtz energy relation

$$\psi(P,\varepsilon) = \psi_P(P) + \frac{1}{2}Y\varepsilon^2 - a_1\varepsilon P - a_2\varepsilon P^2.$$

The Gibbs energy is then given by

$$G(E,\sigma,P,\varepsilon) = \psi(P,\varepsilon) - EP - \sigma\varepsilon \tag{2}$$

where $\sigma\varepsilon$ incorporates the elastic energy. Note that Y denotes the Young's modulus and a_1 and a_2 are ferroelastic coupling coefficients associated with linear piezoelectric and quadratic electrostrictive effects.

1) Polarization Kernel—Negligible Thermal Activation: In the case of negligible thermal activation, the local average polarization kernel $\overline{P}$ is determined from the conditions

$$\frac{\partial G}{\partial P} = 0, \qquad \frac{\partial^2 G}{\partial P^2} > 0.$$

Applying these conditions to (1) yields the piecewise linear E–P relation

$$\overline{P}(E) = \frac{1}{\eta}E + P_R\delta \tag{3}$$

where $\delta = -1$ for negatively oriented dipoles and $\delta = 1$ for those with positive orientation. To specify δ, and hence, $\overline{P}$, in terms of the initial dipole configurations and previous switches, we let $\delta_0 = \pm 1$ designate the initial dipole orientation and take

$$[\overline{P}(E;E_c,\delta_0)](t) = \begin{cases} \frac{E(t)}{\eta} + P_R\delta_0, & \tau = \emptyset \\ \frac{E(t)}{\eta} - P_R, & \tau \neq \emptyset \text{ and } E(\max\tau) = -E_c \\ \frac{E(t)}{\eta} + P_R, & \tau \neq \emptyset \text{ and } E(\max\tau) = E_c. \end{cases} \tag{4}$$

Here $\emptyset$ denotes the empty set and the set of transition times is designated by

$$\tau = \{t \in (0, t_f] \mid E(t) = -E_c \text{ or } E(t) = E_c\}$$

where t_f denotes the final time under consideration.

The local coercive field

$$E_c = \eta(P_R - P_I) \tag{5}$$

quantifies the field at which the negative well ceases to exist and, hence, a dipole switch occurs.

2) Polarization Kernel—Thermal Activation: If thermal activation is significant, dipoles can achieve the thermal energy required to switch in advance of the minimum Gibbs energy so the relative thermal energy kT/V and Gibbs energy G must be balanced through Boltzmann principles. The probability density for achieving an energy level G is given by

$$\mu(G) = Ce^{-GV/kT} \tag{6}$$

where k is Boltzmann's constant, V is a reference volume, and C is a constant that is selected so that when $\mu(G)$ is integrated over all possible dipole orientations, a probability of unity is achieved. If we let 2ϵ be the separation between possible polarization states around P_0, the probabilities of reaching a polarization state having sufficient energy to switch orientations are given by

$$\begin{aligned} r_{+-} &= \frac{\int_{P_0-\epsilon}^{P_0+\epsilon} e^{-G(E,P)V/kT}dP}{\int_{P_0-\epsilon}^{\infty} e^{-G(E,P)V/kT}dP} \\ r_{-+} &= \frac{\int_{P_0-\epsilon}^{P_0+\epsilon} e^{-G(E,P)V/kT}dP}{\int_{-\infty}^{P_0+\epsilon} e^{-G(E,P)V/kT}dP}. \end{aligned} \tag{7}$$

The likelihoods of reaching the required energy and, thus, of the dipoles switching from a positive to a negative orientation and conversely are then

$$p_{+-} = \frac{r_{+-}}{\mathcal{T}(T)}, \qquad p_{-+} = \frac{r_{-+}}{\mathcal{T}(T)} \tag{8}$$

where $\mathcal{T}(T)$ is the relaxation time at temperature T. The fractions of dipoles in each orientation evolve according to the ordinary differential equations

$$\begin{aligned} \frac{dx_+}{dt} &= -p_{+-}x_+ + p_{-+}x_- \\ \frac{dx_-}{dt} &= -p_{-+}x_- + p_{+-}x_+. \end{aligned}$$

The expected polarizations due to positively and negatively oriented dipoles are

$$\begin{aligned} \langle P_+ \rangle &= \frac{\int_{P_0+\epsilon}^{\infty} Pe^{-G(E,P,T)V/kT}dP}{\int_{P_0+\epsilon}^{\infty} e^{-G(E,P,T)V/kT}dP} \\ \langle P_- \rangle &= \frac{\int_{-\infty}^{P_0-\epsilon} Pe^{-G(E,P,T)V/kT}dP}{\int_{-\infty}^{P_0-\epsilon} e^{-G(E,P,T)V/kT}dP}. \end{aligned} \tag{9}$$

The local average polarization is subsequently given by

$$\overline{P} = x_+\langle P_+ \rangle + x_-\langle P_- \rangle. \tag{10}$$

In the manner detailed in [36], the evaluation of the integrals in (7) and (9) can be simplified through approximations employing the inflection points $\pm P_I$ rather than the unstable equilibrium P_0. It is also shown in [25] and [36] that the kernel $\overline{P}$ given by (9) converges to (3) or (4) in the limit $kT/V \to 0$ of negligible thermal activation.

B. Global Constitutive Relations

For homogeneous compounds with uniform effective fields E_e, the local lattice relations (3), (4), or (10) can be extrapolated throughout the material to provide global constitutive relations. This yields the nearly instantaneous transitions at coercivity that are associated with certain single crystal compounds—e.g., the hysteresis kernels depicted in Fig. 4 provide a reasonable characterization of the single crystal $BaTiO_3$ behavior shown on pages 72–76 of [17]—but provide a poor characterization of the mollified transition behavior of general ferroelectric compounds. To incorporate the effects of material nonhomogeneities, polycrystallinity, and variable effective fields $E_e = E + E_I$, we assume that the interaction field E_I, due to neighboring dipoles and certain electromechanical interactions [1], and local coercive field E_c given by (5), are manifestations of underlying distributions rather than constants. If we designate the associated densities by ν_1 and ν_2, the macroscopic field-polarization behavior is quantified by the relation

$$P(E) = \int_0^{\infty}\int_{-\infty}^{\infty} \overline{P}(E + E_I; E_c, \xi) \times \nu_1(E_c)\nu_2(E_I)dE_I dE_c \tag{11}$$

where the kernel $\overline{P}$ is given by (3) or (4) if relaxation effects due to thermal activation are negligible or (10) if thermal relaxation is included in the formulation.

We note that instead of distributing E_c, one could alternatively consider P_I or P_R as manifestations of underlying distributions where the relationship between the three variables is quantified by (5). We chose to distribute E_c because of the input nature of the field.

As detailed in [27], the densities ν_1 and ν_2 are assumed to satisfy the physical criteria:

1) $\nu_1(x)$ defined for $x > 0$;
2) $(-x) = \nu_2(x)$;
3) $|\nu_1(x)| \le c_1 e^{-a_1 x}, \qquad |\nu_2(x)| \le c_2 e^{-a_2|x|}$ (12);

for positive c_1, a_1, c_2, a_2. The restricted domain in 1) reflects the fact that the coercive field E_c is positive, whereas the symmetry enforced in the interaction field through 2) yields the symmetry observed in low-field Rayleigh loops. Hypothesis 3) incorporates the physical observation that the coercive and interaction fields decay as a function of distance and guarantees that integration against the piecewise linear kernel yields finite polarization values.

By employing numerical integration routines tailored to the infinite domains or truncated intervals resulting from the decay

criteria (12), the integrals in (11) can be approximated to obtain the discretized model

$$P(E) = \sum_{i=1}^{N_i} \sum_{j=1}^{N_j} \overline{P}(E + E_{I_j}; E_{c_i}, \xi_j) \nu_1(E_{c_i}) \nu_2(E_{I_j}) v_i w_j. \tag{13}$$

Specific choices for the weights v_i, w_j, and abscissas E_{e_j}, and E_{c_i} are detailed in [25] and [36].

Techniques for identifying the densities ν_1 and ν_2 are illustrated in [27]. For certain applications, reasonable accuracy is provided by *a priori* functions satisfying the physical criteria (12) and having a small number of parameters to be estimated through least squares fits to data—e.g., variances and means in normal and lognormal relations. For more general applications requiring high accuracy for a wide range of operating conditions, the $N_i + N_j$ discretized density values $\nu_1(E_{c_i})$ and $\nu_2(E_{I_j})$ can be estimated through least squares techniques.

To obtain an elastic constitutive relation, the equilibrium condition $\partial G/\partial \varepsilon = 0$ is invoked to obtain

$$\sigma = Y\varepsilon - a_1 P - a_2 P^2. \tag{14}$$

When $P = 0$, (14) reduces to Hooke's law. To incorporate internal damping, we posit that when $P = 0$, stress is proportional to a linear combination of strain and strain rate (Kelvin-Voigt damping hypothesis). Finally, we note that the PZT stage mechanisms are poled and, hence, operate about the remanence polarization $P = P_R$ rather than the depoled state $P = 0$. This yields the constitutive relation

$$\sigma = Y\varepsilon - c_D\dot{\varepsilon} - a_1(P - P_R) - a_2(P - P_R)^2 \tag{15}$$

where c_D is the Kelvin–Voigt damping parameter. The combination of the field-polarization model (11) or (13) and the electromechanical relation (15) are employed in Section IV to construct a lumped model for a stacked PZT actuator operating in hysteretic and nonlinear regimes.

C. Attributes and Implementation of the Field-Polarization Relations

The model formulation (11) resembles that of a Preisach model in the sense that it is comprised of an infinite combination of kernels and densities, and it is shown in [25] and [33] that the homogenized energy framework can be interpreted as providing an energy basis for certain extended Preisach models. However, the energy framework differs from the classical Preisach framework, characterized by the properties of congruency and deletion, in five aspects which prove crucial for both material characterization and model-based control design. 1) The first is the energy basis of the model—formulation through energy analysis provides a low-order model which, for certain density choices, has parameters that can be physically correlated with properties of the data. 2) Due to the energy basis of the framework, stress and temperature-dependencies are incorporated in the basis or kernel in the new model (e.g., see [2] and [21]) whereas they enter the weights in the Preisach formulation. Because they are incorporated in the kernel, the model automatically incorporates these effects which eliminates the necessity of vector-valued weights or lookup tables. From the perspective of implementation, this indicates that only one set of parameters must be identified for the proposed model and no switching between parameter sets is required during operation. This significantly augments the efficiency of characterization and control algorithms employing the model. 3) The incorporation of relaxation mechanisms through the energy basis provides the framework with the property that it accommodates nonclosure or nondeletion properties in accordance with measured material properties. In this case, the framework provides an energy basis for certain extended Preisach formulations based on Arrhenius relations [8]. 4) Derivation of the theory from Ising principles yields kernels or hysterons which accommodate the noncongruency observed for certain materials and operating regimes. This is in contrast to input and output-dependent (moving) Preisach formulations which incorporate noncongruency through input or output-dependent densities. 5) The model automatically incorporates reversible polarization mechanisms for small ac field excursions about a fixed dc value—hence, it accurately characterizes reversible material behavior following field reversal without the extensions required for Preisach formulations.

We note that whereas several of these properties have been incorporated in extended Preisach models for magnetic materials (e.g., see [8]), analogous extensions have not yet been made for ferroelectric Preisach models.

The efficient implementation of the discretized model (13) is crucial for real-time control implementation. It is illustrated in [25] and [27] that for the thermally inactive kernel $\overline{P}$ given by (3) or (4), reformulation of the `if-then` statements in terms of componentwise matrix multiplication yields algorithms that allow multiloop simulations to run in the order of seconds. Implementation algorithms for regimes in which the kernel (10) is used to incorporate thermal relaxation are addressed in [3]. By computing and storing exponential expressions resulting from the Boltzmann relation (6), the relaxation algorithms also permit multiloop simulations to be run in 1–2 s on present laptop and workstation architectures. Hence, both cases are sufficiently efficient to facilitate real-time control implementation. Matlab codes implementing the algorithms are available at the website http://www4.ncsu.edu/~rsmith/Smart_Material_Systems/Chapter2 associated with [25].

Attributes of the discretized model (13) utilizing the thermally active kernel (10), are illustrated in Fig. 5. The relaxation behavior is readily apparent between 40 and 50 s, where it is noted that there is significant polarization change despite the fact that the input field is held constant. This simulates the creep behavior measured in AFM stages where one component is held fixed, while a sweep is performed with the other, and it demonstrates the necessity of incorporating relaxation mechanisms for comprehensive AFM characterization and control.

III. Inverse Relation Between Polarization and Field

The model (11) and discretized model (13) quantify the relation between input fields and the polarization generated in ferroelectric materials. To construct an inverse filter of the type illustrated in Fig. 3, it is necessary to quantify the inverse P–E

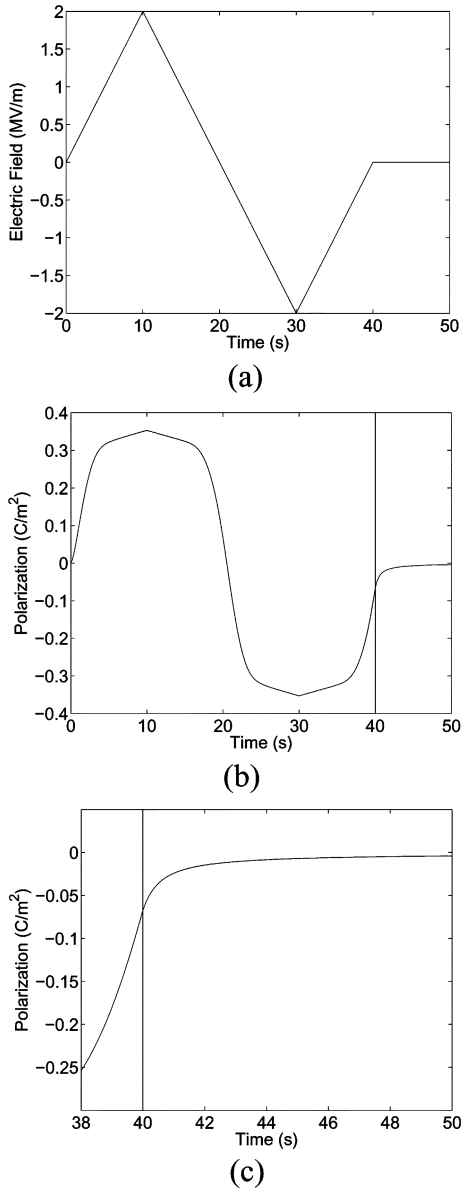

Fig. 5. (a) Input field E and (b) polarization P given by (13) with the thermally active kernel (10). The vertical line indicates the time at which the electric field is held constant. (c) Detailed view of the creep component of the simulation.

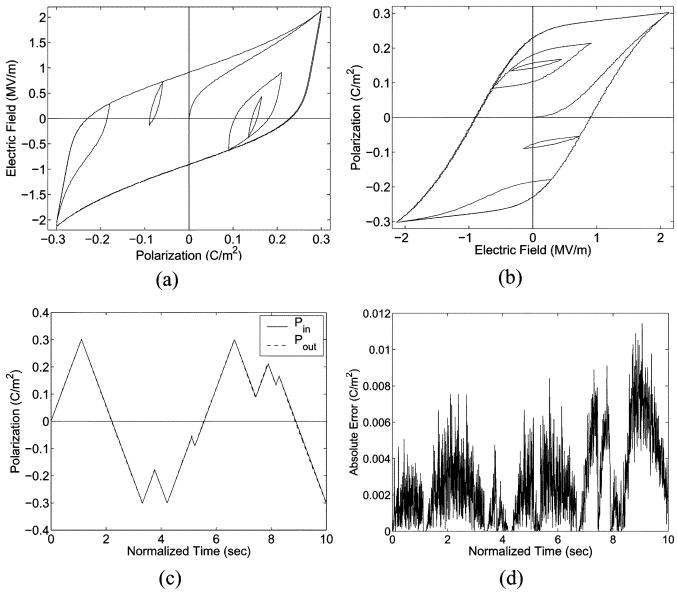

Fig. 6. (a) Inverse relation $P_{\rm in}$-$E_{\rm out}$ given by Algorithm 1. (b) Forward relation $E_{\rm out}$-$P_{\rm out}$ from model (13). (c) Comparison between $P_{\rm in}$ and $P_{\rm out}$. (d) Absolute error $|P_{\rm in}-P_{\rm out}|$ for complete inversion process depicted in Fig. 3.

relation. We summarize here an algorithm which accomplishes this when the E–P relation is assumed monotone and illustrate the filtering process through a numerical example. Extension of the algorithm to accommodate the nonmonotone field-displacement behavior shown in Fig. 2 is addressed in Section V.

The first step in the construction of an inverse filter involves the determination of an initial (E_0, P_0) value. This is typically done with $E_0 = 0$ so that $P_0 = \pm P_R$ is the positive or negative remanence value or $P_0 = 0$ for depoled materials. The values of $\pm P_R$ can be computed using the forward model (11) or (13) by applying a sufficiently large field $\pm E_{\max}$ so that all dipoles have switched and then stepping back to $E = 0$. For a specified value of P, monotonicity in the E–P relation is exploited and the forward model is subsequently advanced until the prescribed polarization is crossed. Interpolation is then used to specify a final field value corresponding to the prescribed polarization. This process is outlined in Algorithm 1, where specified polarization values are designated by $\{P_k^*\}$ and computed values by $\{P_k\}$ for $k = 1, \ldots N_k$. Adaptive stepsizes can be implemented by halving the nominal stepsize $E_{\rm step}$ if the number of iterations exceeds a specified counter.

Algorithm 1

for $k = 2 : N_k$
  Specify $E_{\rm step} > 0$ as fixed or adaptive
  $dP = P_k^* - P_{k-1}^*$
  $\Delta E = dP \cdot E_{\rm step}$
  $E_{\rm tmp} = E_{k-1}$, $P_{\rm tmp} = P_{k-1}$
  while $\mathrm{sgn}(dP) \cdot (P_k^* - P_{\rm tmp}) >= 0$
    $E_{\rm tmp} = E_{\rm tmp} + \Delta E$
    $P_{\rm tmp}$ given by **(13)**
  end
  E_k given by linear interpolation
end

The flexibility and robustness provided by the inverse Algorithm 1 are illustrated in Fig. 6 for regimes with moderate thermal relaxation. The specified input polarization plotted in Fig. 6(c) is employed as input to Algorithm 1 to yield the P–E relation plotted in Fig. 6(a). At each time step, the resulting field value is then employed as input to the forward model (13) to yield the E–P curve shown in Fig. 6(b). These output polarization values $P_{\rm out}$ are compared with inputs $P_{\rm in}$ in Fig. 6(c) and the absolute errors $|P_{\rm in} - P_{\rm out}|$ are plotted in Fig. 6(d).

From these results, a number of conclusions can be drawn. 1) We first note that the model and its inverse provide the capability for characterizing a wide range of symmetric and biased minor loop behavior—e.g., see [25], [27], and [36]. 2) The composition of the inverse and model in the manner depicted in

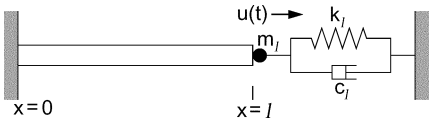

Fig. 7. Rod geometry used when modeling the stacked PZT actuator employed in the AFM stage depicted in Fig. 1(a).

Fig. 3 can effectively linearize the nonlinear transducer behavior with the numerical accuracy $|P_{\text{in}} - P_{\text{out}}|$ limited only by the stepsize dP. Whereas, the accuracy in a physical system will be diminished due to modeling error, linearization in this manner can significantly improve control authority since less control effort is focused on unmodeled or nonlinear dynamics. This forms the crux of various linear control designs [18], [19]. 3) Although faster implementation algorithms can be constructed for the inversion process [10], the algorithm described here is highly robust and avoids the potential for losing track of the memory incorporated in the model. Furthermore, the use of adaptive stepsizes ΔE ensures that Algorithm 1 is approximately a factor of two slower than forward algorithms which is reasonable for physical implementation.

IV. Lumped Model for the Stacked Actuator

The constitutive relation (15) quantifies the electromechanical behavior of piezoceramic materials operating below the coercive stress σ_c where ferroelastic switching commences. In this section, we use this relation to construct a macroscopic model for the stacked PZT rod employed as an AFM stage in the manner depicted in Fig. 1(a). Whereas this illustrates macroscopic model development for a specific application, similar principles hold for other transducer designs—e.g., see [25].

We assume that the stacked actuator or rod has length ℓ, cross-sectional area A, density ρ, Young's modulus Y, and Kelvin-Voigt damping parameter c_D. We also assume that the end at $x = 0$ is fixed, whereas the end at $x = \ell$ is subjected to inertial, elastic, and damping forces associated with the stage mechanisms. Because material properties and forces along the length of the rod are uniform, we consider a lumped model quantifying the displacement $u(t)$ at $x = \ell$. The validity of the lumped ODE model as compared with a distributed PDE model is established in [28]. The geometry, mass m_ℓ, stiffness k_ℓ, and damping mechanisms c_ℓ associated with the end-forces at $x = \ell$ are depicted in Fig. 7.

From the assumption of uniform stresses and strains through the length of the rod, it follows that:

$$\varepsilon(t) = \frac{u(t)}{\ell}$$

in the stress relation (15). Balancing the forces σA for the rod with those of the stage mechanisms yields the lumped model

$$\rho A \frac{d^2u}{dt^2}(t) + \frac{c_D A}{\ell}\frac{du}{dt}(t) + \frac{YA}{\ell}u(t) - Aa_1[P(E(t)) - P_R] - Aa_2[P(E(t)) - P_R]^2 = -m_\ell \frac{d^2u}{dt^2}(t) - c_\ell \frac{du}{dt}(t) - ku(t)$$

or, equivalently

$$m\frac{d^2u}{dt^2}(t) + c\frac{du}{dt}(t) + ku(t) = \widetilde{a}_1[P(E(t)) - P_R] + \widetilde{a}_2[P(E(t)) - P_R]^2 \tag{16}$$

where

$$\begin{aligned} m &= \rho A + m_\ell \\ c &= \frac{c_D A}{\ell} + c_\ell \\ k &= \frac{YA}{\ell} + k_\ell \\ \widetilde{a}_1 &= Aa_1 \\ \widetilde{a}_2 &= Aa_2 \end{aligned}$$

and the initial conditions are $u(0) = u_0$ and $(du/dt)(0) = u_1$. The polarization P is specified by the model (11) or discretized model (13).

The model can also be written as the first-order system

$$\begin{aligned} \dot{\vec{u}}(t) &= A\vec{u}(t) + \vec{\mathcal{P}}(E(t)) \\ \vec{u}(0) &= \vec{u}_0 \end{aligned} \tag{17}$$

where $\vec{u}(t) = [u(t), \dot{u}(t)]^T$, $\vec{u}(0) = [u_0, u_1]^T$, and

$$A = \begin{bmatrix} 0 & 1 \\ -\frac{k}{m} & -\frac{c}{m} \end{bmatrix}$$

$$\vec{\mathcal{P}}(E(t)) = \frac{1}{m}\left[\widetilde{a}_1(P(E(t)) - P_R) + \widetilde{a}_2(P(E(t)) - P_R)^2\right] \times \begin{bmatrix} 0 \\ 1 \end{bmatrix}.$$

This formulation proves advantageous in Section V when establishing notation used in the construction of the inverse algorithm.

The accuracy of the framework is illustrated in Fig. 8, where the lumped model (16), with P specified by (13) using the thermally active kernel $\overline{P}$ given by (10), is used to characterize the frequency-dependent dynamics of the PZT stacked actuator employed in the AFM stage depicted in Fig. 1(a). When constructing the polarization model, the general densities ν_1 and ν_2 were identified using the least squares techniques detailed in [27]. It is noted that the combined model quantifies the hysteresis, internal damping, and dynamic effects observed as frequencies are increased. Additional details regarding the construction and validation of the stacked actuator model for the AFM stage are provided in [28], where it is demonstrated that a loss of accuracy results if thermal activation mechanisms are neglected in the model. Additional examples demonstrating properties of the model for characterizing hysteresis in various PZT compounds can be found in [25]–[27], and [36].

V. Inverse Relation Between Displacements and Fields

The inversion algorithm summarized in Section III relies on the monotonicity of the E–P relation. As illustrated in Fig. 2, this property is not shared by the E-u relation as frequencies are increased so we develop here an extended inversion algorithm

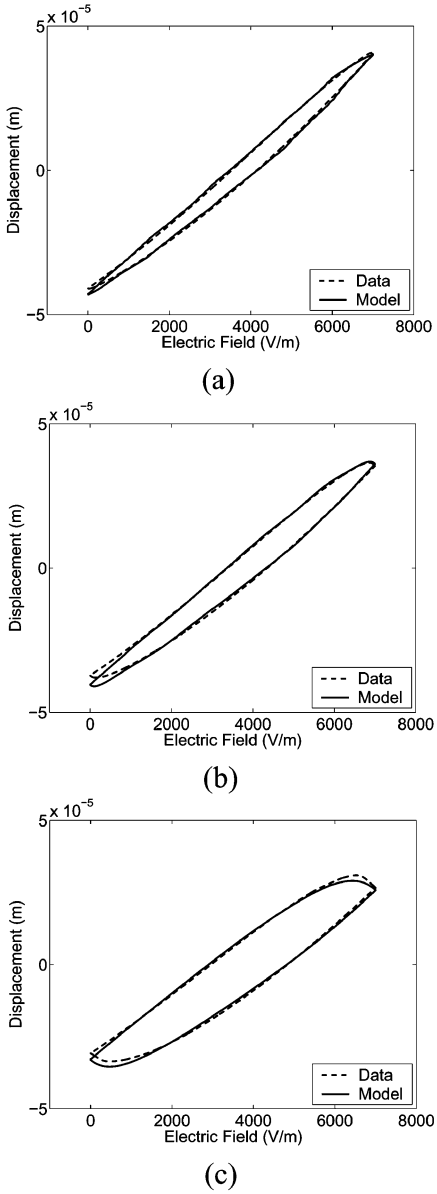

Fig. 8. Characterization of AFM field-displacement behavior with sample rates of: (a) 0.279; (b) 5.58; and (c) 27.9 Hz.

which incorporates this nonmonotone behavior. The crux of the modification focuses on the accommodation of dynamic effects in the E-u behavior.

To establish notation used when quantifying dynamic effects, we employ modified semigroup notation to define solution values

$$\begin{aligned} u_{k+1} &= u(t_{k+1}, t_k, E, \vec{u}_k) \\ &= Ce^{A(t_{k+1}-t_k)}\vec{u}_k + C\int_{t_k}^{t_{k+1}} e^{A(t_{k+1}-s)}\vec{\mathcal{P}}(E(s))ds \\ \widetilde{u}_{k+1} &= u(t_{k+1}, t_k, E_k, \vec{u}_k) \\ &= Ce^{A(t_{k+1}-t_k)}\vec{u}_k + C\int_{t_k}^{t_{k+1}} e^{A(t_{k+1}-s)}\vec{\mathcal{P}}(E_k)ds \end{aligned} \tag{18}$$

where $C = [0,1]$ and $E_k = E(t_k)$. Hence, u_{k+1} is the solution to (16) or (17) with the electromechanical force applied

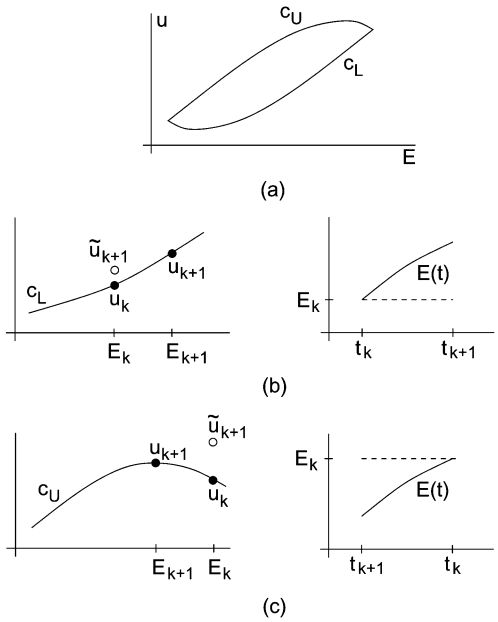

Fig. 9. Nonmonotone behavior of the field-displacement relation measured at 27.9 Hz, as shown in Fig. 2(c). Solution values $\widetilde{u}_{k+1}$ and u_{k+1}, respectively, due to field inputs E_k and $E(t)$ on the (b) lower loop c_L and (c) upper loop c_U of the curve.

throughout the time interval $[t_k, t_{k+1}]$, whereas $\widetilde{u}_{k+1}$ denotes the displacement of the rod at $x = \ell$ with the force maintained constant at the kth value throughout the interval $[t_k, t_{k+1}]$ as depicted in Fig. 9. The definition of u_k is similar to that of u_{k+1}.

The upper and lower hysteresis curves are denoted by

$$c_L = \left\{(E,u) \mid \frac{dE}{dt} \geq 0\right\}$$
$$c_U = \left\{(E,u) \mid \frac{dE}{dt} \leq 0\right\}.$$

Due to dynamic (inertial) effects, it is observed that

$$\begin{aligned} \widetilde{u}_{k+1} &\leq u_{k+1} \text{ on } c_L \\ \widetilde{u}_{k+1} &\geq u_{k+1} \text{ on } c_U \end{aligned} \tag{19}$$

as depicted in Fig. 9(b) and (c). To motivate the relation on c_L, we note that (18) yields

$$u_{k+1} - \widetilde{u}_{k+1} = C\int_{t_k}^{t_{k+1}} e^{A(t_{k+1}-s)}\left[\vec{\mathcal{P}}(E(s)) - \vec{\mathcal{P}}(E_k)\right]ds. \tag{20}$$

We now establish that the right-hand side (RHS) of (20) is nonnegative given that the monotonicity of the E-P relation implies that $\vec{\mathcal{P}}(E(s)) - \vec{\mathcal{P}}(E_k) \geq 0$ for $s \geq t_k$. We first note that the Cayley–Hamilton theorem dictates that $e^{A(t_{k+1}-s)} = \alpha_0 I + \alpha_1 A$. Furthermore, it follows from the definitions of C and $\vec{\mathcal{P}}(E(t))$ that only the (1,2) entry of $e^{A(t_{k+1}-s)}$ contributes to the RHS of (20). Moreover, it follows from the definition of A that the (1,2) entry of $e^{A(t_{k+1}-s)}$ is simply α_1.

To determine α_1, we note that there are two possibilities for the eigenvalues of A: 1) both are real, distinct, and negative and 2) they are a conjugate pair with negative real part. We consider

the first case where the eigenvalues satisfy $\lambda_2 < \lambda_1 < 0$. It follows from the Cayley–Hamilton theorem that

$$e^{\lambda_1(t_{k+1}-s)} = \alpha_0 + \alpha_1\lambda_1$$
$$e^{\lambda_2(t_{k+1}-s)} = \alpha_0 + \alpha_1\lambda_2$$

so that

$$\alpha_1 = \frac{e^{\lambda_1(t_{k+1}-s)} - e^{\lambda_2(t_{k+1}-s)}}{\lambda_1 - \lambda_2} > 0.$$

Similar analysis holds for the second case. Thus, the integrand $Ce^{A(t_{k+1}-s)}[\vec{\mathcal{P}}(E(s)) - \vec{\mathcal{P}}(E_k)]$ of (20) is nonnegative and, consequently, so is the integral. As a result, $u_{k+1} - \widetilde{u}_{k+1} \geq 0$ or equivalently $\widetilde{u}_{k+1} \leq u_{k+1}$. The argument for c_U is analogous.

In the inverse algorithm used to specify the u-E relation given data values $\{u_k^*\}$, $k = 1, \ldots, N_k$, the inequalities (19) are applied to either the exact or discretized solution of (16) to determine the appropriate sign of ΔE when implementing the polarization component (13) of the model. The notation $u_{\rm tmp}$ and $\widetilde{u}_{\rm tmp}$ designate either the exact or approximate solutions to (13) having the interpretation specified in (18). The resulting inversion process is outlined in Algorithm 2. Attributes of the algorithm are illustrated in Section VI in the context of experimental open-loop control implementation.

Algorithm 2

for $k = 2 : N_k$
  Specify $E_{\rm step} > 0$ as fixed or adaptive
  Specify Δt
  $\Delta E = \mathrm{sgn}(u_{k+1}^* - \widetilde{u}_{k+1}) \cdot E_{\rm step}$
  $E_{\rm tmp} = E_{k-1}$, $P_{\rm tmp} = P_{k-1}$, $t_{\rm tmp} = t_{k-1}$
  while $\mathrm{sgn}(u_{k+1}^* - \widetilde{u}_{\rm tmp}) \cdot \Delta E >= 0$
    $t_{\rm tmp} = t_{\rm tmp} + \Delta t$
    compute $u_{\rm tmp}$ as true or
      approximate solution to **(16)**
    $E_{\rm tmp} = E_{\rm tmp} + \Delta E$
    $P_{\rm tmp}$ given by **(13)**
  end
  E_k given by linear interpolation
end

VI. Open-Loop Control Implementation

To illustrate the effect of filters employing the inverse model developed in Section V on open-loop tracking performance, we summarize experiments conducted at 0.279 and 27.9 Hz. The trajectory to be tracked consisted of triangle waves having amplitudes of 40.56 and 27.04 μm as shown in Figs. 10–12.

To specify the model, parameters in the polarization model (13) and lumped rod model (16), were estimated through a least squares fit to field-displacement data collected at 0.279, 5.58, and 27.9 Hz using the techniques detailed in [27]. This yielded model fits similar to those shown in Fig. 8. The model with these

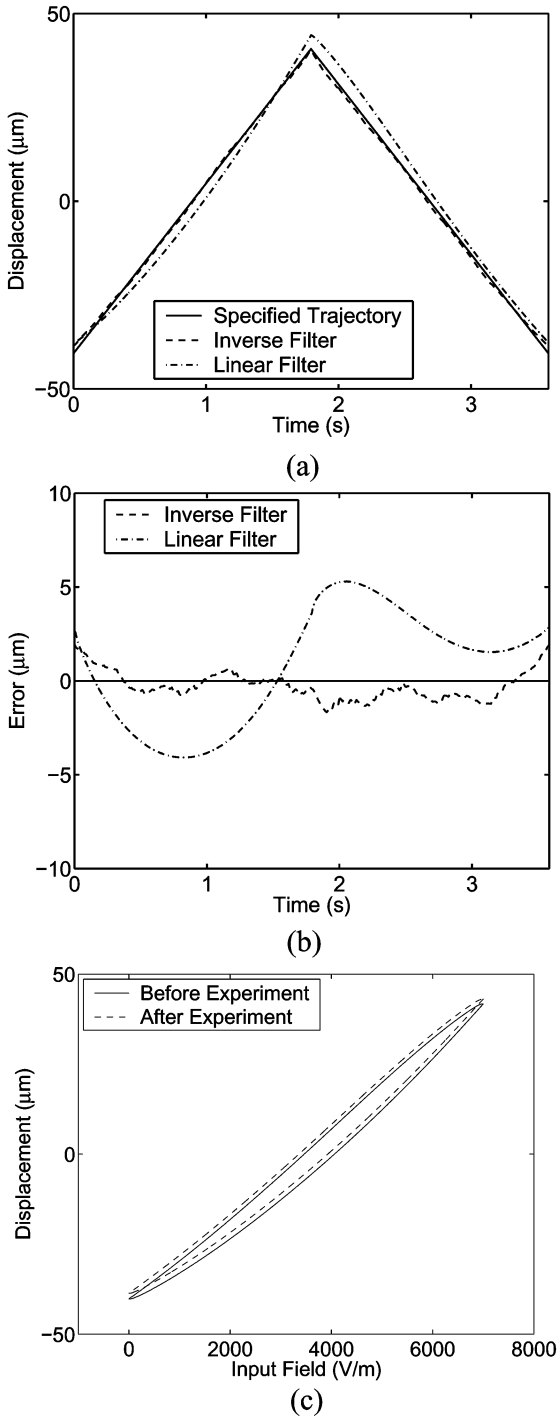

Fig. 10. Tracking performance utilizing the model-based inverse filter of Section V and a static linear filter at 0.279 Hz and amplitude of 40.56 μm. (a) Specified trajectory and tracking provided by the inverse and linear filters, and (b)errors obtained with the two filters. (c) Field-displacement data measured before and after the open-loop control experiment.

parameters was then used to construct an inverse filter using Algorithm 2 of Section V. In a series of experiments, the specified trajectories were input to the filter and the resulting field was applied to the AFM stage. To provide a metric for comparison, a second input field for each case was determined through a linear scaling of the field-displacement relation. This static linear filter

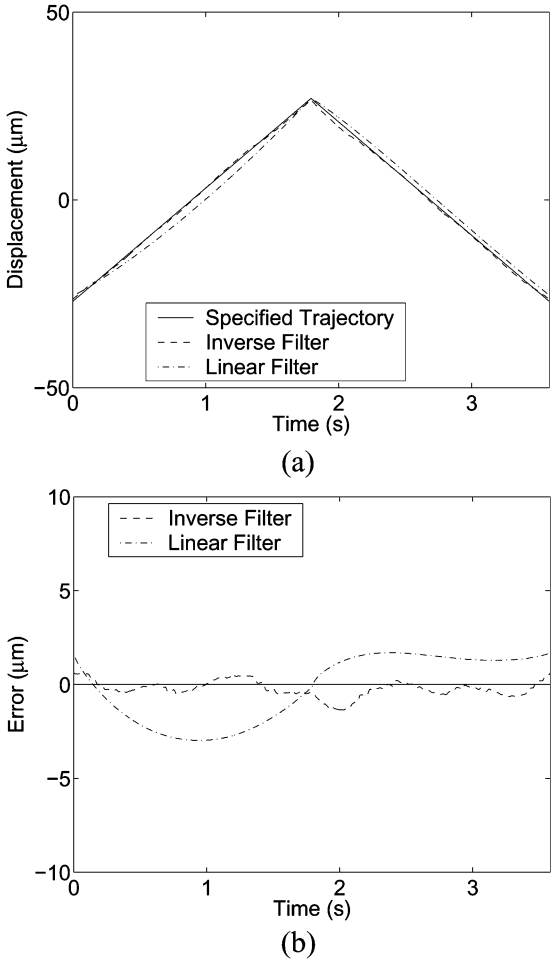

Fig. 11. Tracking performance utilizing the model-based inverse filter of Section V and a static linear filter at 0.279 Hz and amplitude of 27.04 μm. (a) Specified trajectory and tracking provided by the inverse and linear filters and (b) errors obtained with the two filters.

accommodated the scaling difference between inputs and outputs but neglected inherent hysteresis, constitutive nonlinearities, internal damping losses, and interial dynamics.

The specified and achieved trajectories, errors, and selected hysteresis plots for the combinations; 1) 0.279 Hz, 40.56 μm amplitude; 2) 0.279-Hz, 27.04-μm amplitude; and 3) 27.9-Hz, 27.04-μm amplitude are plotted in Figs. 10–12. At 0.279 Hz, the filtered design provides only marginally improved accuracy due to the low degree of hysteresis, damping losses, and inertial dynamics. However, for the response at 27.9 Hz which exhibits significant losses, the inverse filter provides a significant increase in accuracy and yields errors that are approximately a factor of 10 smaller than the errors obtained with the static linear filter. This illustrates the advantage of incorporating the frequency-dependent model inverse in the control design. We note that the same model parameters were employed in each case, thus, illustrating the capability of the model and model-based inverse to compensate for the frequency-dependent hysteresis, internal damping losses, and inertial dynamics.

The primary source of errors in the filtered design is variable between experiments as illustrated by the variation in the hysteresis plots measured at the two frequencies before and after

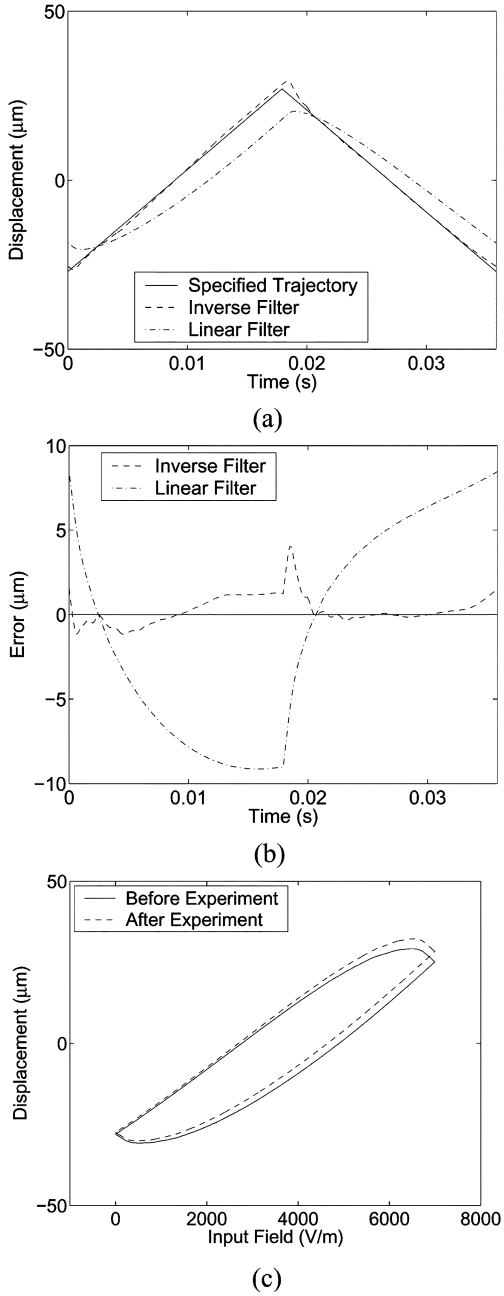

Fig. 12. Tracking performance utilizing the model-based inverse filter of Section V and a static linear filter at 27.9 Hz and amplitude of 27.04 μm. (a) Specified trajectory and tracking provided by the inverse and linear filters, and (b) errors obtained with the two filters. (c) Field-displacement data measured before and after the open-loop control experiment.

the open-loop control experiments. This illustrates one reason feedback is necessary in final control designs.

The results in Figs. 10–12 compare the tracking accuracy obtained in experiments using a linear static filter and an inverse filter based on the model (16) which incorporates internal damping, inertial dynamics, and hysteresis. An intermediate alternative is to construct a linear, dynamic filter based on inversion of the model

$$m\frac{d^2u}{dt^2}(t) + c\frac{du}{dt}(t) + ku(t) = \gamma E(t) \tag{21}$$

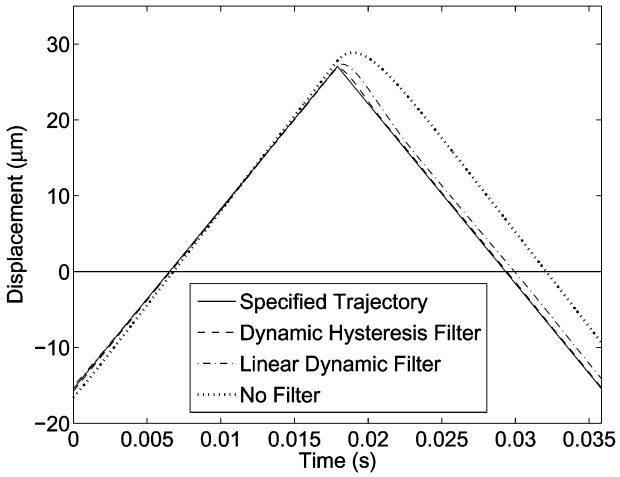

Fig. 13. Numerical simulation of tracking performance obtained with the dynamic hysteresis filter resulting from inverting the model (16), the linear dynamic filter resulting from (21), and no inverse filter.

where γ is an electromechanical coupling coefficient, which incorporates damping and inertial effects but neglects hysteresis. Because the three mechanisms which contribute to the frequency-dependent losses exhibited in Figs. 10(c) and 12(c) are inherently coupled, it is impossible to separate them in experiments for the purpose of parameter estimation. Hence, when constructing a linear dynamic filter, we employed the parameter values for m, c, and k obtained for the dynamic hysteresis model (16) which yielded the fits shown in Fig. 8.

Numerical simulations of the tracking performance obtained with the filter obtained by inverting the dynamic model (16) with hysteretic inputs, the linear dynamic filter obtained by inverting (21), and no filter are illustrated in Fig. 13. The respective absolute errors at T =0.02 s of 0.3421, 2.0222, and 6.0038 μm demonstrate the relative performance of the three techniques. At that time, the linear dynamic filter provides a three-fold improvement in accuracy over the unfiltered case but is nearly six times less accurate than the dynamic hysteresis filter which incorporates all three loss mechanisms. Whereas the degree of accuracy provided by the linear dynamic filter varies throughout the time interval, it is significantly less accurate than the hysteresis filter. Furthermore, the computational cost associated with implementing the dynamic hysteresis filter is commensurate with that of the linear dynamic filter. For high accuracy tracking, we, thus, focus on the dynamic hysteresis filter based on inversion of the model (16).

VII. Concluding Remarks

This paper addresses the development, implementation, and experimental validation of a model-based inverse filter to accommodate hysteresis and constitutive nonlinear inherent to the field-polarization and field-displacement behavior of ferroelectric materials. The nonlinear hysteresis effects are quantified using a previously developed framework consisting of energy relations at the lattice level in combination with stochastic homogenization techniques to provide low-order macroscopic constitutive relations. The development of a lumped transducer model based on these constitutive relations is illustrated in the context of a PZT stage for an AFM. The inverse displacement-field model exploits monotonicity in the E–P relation, the efficiency of forward E–P algorithms, and dynamic properties of the transducer model.

To illustrate attributes of the inverse displacement-field algorithm, it was employed as a filter in open-loop tracking experiments with an AFM stage. These experiments illustrate that at low frequencies, where hysteresis and constitutive nonlinearities are minimal, incorporation of the inverse filter provides only marginal improvement in tracking accuracy as compared with a linear filter. However, at higher frequencies where hysteresis becomes significant, the inverse filter yields an approximately tenfold improvement in accuracy compared with the linear filter, thus, maintaining tracking accuracy even though the transducer is operating in highly hysteretic and nonlinear regimes. Linearization of the electromechanical behavior in this manner reduces the degree to which feedback mechanisms must expend energy linearizing the transducer response and increases control authority for stabilization or tracking.

We note that a significant advantage of the energy-based model is the fact that it provides a unified framework for characterizing hysteresis and constitutive nonlinearities in ferroelectric, ferromagnetic, and ferroelastic (e.g., SMA) compounds [34], [35]. One facet of present investigations focuses on the extension and implementation of the inverse filtering techniques for the latter two classes of compounds.

Present investigations are also focused on the development of robust feedback control designs which employ the inverse filters to linearize transducer dynamics. Initial investigations focused on the numerical implementation of these energy-based inverse filters for magnetic transducers will be reported in [20] and the experimental implementation of feedback designs exploiting the filters are under present investigation.

References

[1] J. C. Anderson, *Dielectrics*. New York: Reinhold, 1964.
[2] B. L. Ball, R. C. Smith, S.-J. Kim, and S. Seelecke, "A stress-dependent hysteresis model for ferroelectric materials," *J. Intell. Mater. Syst. Structures*, to be published.
[3] T. Braun and R. C. Smith, "An efficient implementation algorithm for a homogenized energy model with thermal relaxation," in *Proc. SPIE, Smart Structures Mater.*, 2005, pp. 377–387.
[4] W. Chen and C. S. Lynch, "A model for simulating polarization switching and AF-F phase changes in ferroelectric ceramics," *J. Intell. Mater. Syst. Structures*, vol. 9, pp. 427–431, 1998.
[5] ——, "A micro-electro-mechanical model for polarization switching of ferroelectric materials," *Acta Materialia*, vol. 46, no. 15, pp. 5303–5311, 1998.
[6] D. Croft, G. Shed, and S. Devasia, "Creep, hysteresis, and vibration compensation for piezoactuators: Atomic force microscopy application," *J. Dyn. Syst., Meas., Contr.*, vol. 23, pp. 35–43, 2001.
[7] A. Daniele, S. Salapaka, M. V. Salapaka, and M. Dahleh, "Piezoelectric scanners for atomic force microscopes: Design of lateral sensors, identification and control," in *Proc. Amer. Contr. Conf.*, 1999, pp. 253–257.
[8] E. D. Torre, *Magnetic Hysteresis*. New York: IEEE Press, 1999.
[9] P. Ge and M. Jouaneh, "Modeling hysteresis in piezoceramic actuators," *Precision Eng.*, vol. 17, pp. 211–221, 1995.
[10] A. G. Hatch, "Model development and control design for atomic force microscopy," Ph.D. dissertation, Dept. Math., North Carolina State Univ., Raleigh, 2004.
[11] L. Huang and H. F. Tiersten, "An analytic description of slow hysteresis in polarized ferroelectric ceramic actuators," *J. Intell. Mater. Syst. Structures*, vol. 9, pp. 417–426, 1998.
[12] R. V. Iyer, X. Tan, and P. S. Krishnaprasad, "Approximate inversion of a hysteresis operator with application to control of smart actuators," *IEEE Trans. Autom. Contr.*, vol. 50, no. 6, pp. 778–810, Jun. 2005.

[13] C. M. Landis, "Non-linear constitutive modeling of ferroelectrics," *Current Opinion Solid State Mater. Sci.*, vol. 8, pp. 59–69, 2004.
[14] W. Lu, D.-N. Fang, and K.-C. Hwang, "Nonlinear electric-mechanical behavior and micromechanics modelling of ferroelectric domain evolution," *Acta Materialia*, vol. 47, no. 10, pp. 2913–2926, 1999.
[15] J. A. Main, E. Garcia, and D. V. Newton, "Precision position control of piezoelectric actuators using charge feedback," *J. Guid., Contr., Dyn.*, vol. 18, no. 5, pp. 1068–73, 1995.
[16] J. A. Main, D. Newton, L. Massengil, and E. Garcia, "Efficient power amplifiers for piezoelectric applications," *Smart Mater. Structures*, vol. 5, no. 6, pp. 766–775, 1996.
[17] A. J. Moulson and J. M. Herbert, *Electroceramics: Materials, Properties, Applications*. London, U.K.: Chapman & Hall, 1990.
[18] J. M. Nealis and R. C. Smith, "$\mathcal{H}_\infty$ control design for a magnetostrictive transducer," in *Proc. 42nd IEEE Conf. Dec. Contr.*, 2003, pp. 1801–1806.
[19] ——, "Model-based robust control design for magnetostrictive transducers operating in hysteretic and nonlinear regimes," *IEEE Trans. Contr. Syst. Technol.*, to be published.
[20] W. Oates and R. C. Smith, "Robust control design for nonlinear smart systems," presented at the Smart Structures Mater. Conf., 2005.
[21] J. K. Raye and R. C. Smith, "A temperature-dependent hysteresis model for relaxor ferroelectric compounds," in *Proc. SPIE, Smart Structures Mater.*, 2004, pp. 1–10.
[22] G. Robert, D. Damjanovic, and N. Setter, "Preisach modeling of piezoelectric nonlinearity in ferroelectric ceramics," *J. Appl. Phys.*, vol. 89, no. 9, pp. 5067–5074, 2001.
[23] S. Salapaka, A. Sebastian, J. P. Cleveland, and M. V. Salapaka, "High bandwidth nano-positioner: A robust control approach," *Rev. Scientific Instruments*, vol. 73, no. 9, pp. 3232–3241, 2002.
[24] R. C. Smith, "A nonlinear optimal control method for magnetostrictive actuators," *J. Intell. Mater. Syst. Structures*, vol. 9, no. 6, pp. 468–486, 1998.
[25] ——, *Smart Material Systems: Model Development*. Philadelphia, PA: SIAM, 2005.
[26] R. C. Smith and A. Hatch, "Parameter estimation techniques for nonlinear hysteresis models," in *Proc. SPIE, Smart Structures Mater.*, 2004, pp. 155–163.
[27] R. C. Smith, A. Hatch, B. Mukherjee, and S. Liu, "A homogenized energy model for hysteresis in ferroelectric materials: General density formulation," *J. Intell. Mater. Syst. Structures*, vol. 16, no. 9, pp. 713–732, 2005.
[28] R. C. Smith, A. G. Hatch, T. De, M. V. Salapaka, R. C. H. del Rosario, and J. K. Raye, "Model development for atomic force microscope stage mechanisms," *SIAM J. Appl. Math.*, to be published.
[29] R. C. Smith and C. L. Hom, "Domain wall theory for ferroelectric hysteresis," *J. Intell. Mater. Syst. Structures*, vol. 10, no. 3, pp. 195–213, 1999.
[30] R. C. Smith and Z. Ounaies, "A domain wall model for hysteresis in piezoelectric materials," *J. Intell. Mater. Syst. Structures*, vol. 11, no. 1, pp. 62–79, 2000.
[31] R. C. Smith, Z. Ounaies, and R. Wieman, "A model for rate-dependent hysteresis in piezoceramic materials operating at low frequencies," in *Proc. SPIE, Smart Structures Mater.*, 2000, pp. 128–136.
[32] R. C. Smith and M. Salapaka, "Model development for the positioning mechanisms in an atomic force microscope," *Int. Series Numer. Math.*, vol. 143, pp. 249–269, 2002.
[33] R. C. Smith and S. Seelecke, "An energy formulation for Preisach models," in *Proc. SPIE, Smart Structures and Materials*, 2002, pp. 173–182.
[34] R. C. Smith, S. Seelecke, M. J. Dapino, and Z. Ounaies, "A unified model for hysteresis in ferroic materials," in *Proc. SPIE, Smart Structures Mater.*, 2003, pp. 88–99.
[35] ——, "A unified framework for modeling hysteresis in ferroic materials," *J. Mechan. Phys. Solids*, vol. 34, no. 1, pp. 46–85, 2005.
[36] R. C. Smith, S. Seelecke, Z. Ounaies, and J. Smith, "A free energy model for hysteresis in ferroelectric materials," *J. Intell.t Mater. Syst. Structures*, vol. 14, no. 11, pp. 719–739, 2003.
[37] X. Tan and J. S. Baras, "Modeling and control of hysteresis in magnetostrictive actuators," *Automatica*, vol. 40, no. 9, pp. 1469–1480, 2004.
[38] G. Tao and P. V. Kokotović, *Adaptive Control of Systems with Actuator and Sensor Nonlinearities*. New York: Wiley, 1996.
[39] J. Zhong, S. Seelecke, R. C. Smith, and C. Büskens, "Optimal control of piezoceramic actuators," in *Proc. SPIE, Smart Structures Mater.*, 2003, pp. 264–274.

Andrew G. Hatch received the B.S. degrees in mathematics and physics, the M.S. and the Ph.D. degrees both in applied mathematics from North Carolina State University, Raleigh, in 1996, 2000, and 2004, respectively.

He is presently employed at CNA Corporation.

Ralph C. Smith received the A.B. degree in applied mathematics from Harvard University, Cambridge, OH, in 1983 and the M.S. and Ph.D. degrees in mathematics from Montana State University, Bozeman, in 1987 and 1990, respectively.

From 1990 to 1993, he was a Staff Scientist at the Institute for Computer Applications in Science and Engineering (ICASE) at NASA Langley Research Center, Hampton, VA. In September 1993, he joined the faculty of Mathematics as an Assistant Professor at Iowa State University, Ames. In January 1998, he joined the Department of Mathematics at North Carolina State University, Raleigh, where is presently a Professor. His research interests include smart material applications, numerical analysis, and parameter estimation and control in distributed parameter systems with application to structural, structural acoustic, and aeroacoustic systems.

Tathagata De received the B.Tech.(H) degree in energy engineering (EE) from the Indian Institute of Technology (IIT), Kharagpur, India, in 2000.

He is currently a Research Assistant in the Department of Electrical and Computer Engineering at Iowa State University, Ames. His research interests include fundamental limitations in high speed AFM due to piezo and cantilever dynamics, application of systems theory to nano-positioning and AFM, and noninvasive study of single cell dynamics. He has seven publications in AIP and IEEE journals and conferences which focus on piezoceramic material characterization, nano-positioning, and atomic force microscope (AFM) instrumentation.

Mr. De is a recipient of the President of India Silver Medal as the Best Student in the undergraduate class of Energy Engineering in 2000.

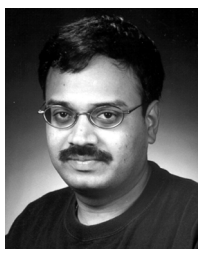

Murti V. Salapaka was born in Andhra Pradesh, India, in 1969. He received the B. Tech. degree in mechanical engineering from the Indian Institute of Technology, in 1991, and the M.S. and Ph.D. degrees in mechanical engineering from the University of California at Santa Barbara, in 1993 and 1997, respectively.

Since 1997, he has been a faculty member in the Electrical and Computer Engineering Department at Iowa State University, Ames. His current research interests include controls for nanotechnology, multiple-objective control, and dynamical systems.